

## RESEARCH ARTICLE SUMMARY

## DNA ORIGAMI

## Absolute and arbitrary orientation of single-molecule shapes

Ashwin Gopinath\*, Chris Thachuk, Anya Mitskovets, Harry A. Atwater, David Kirkpatrick, Paul W. K. Rothemund\*

**INTRODUCTION:** Molecular and particulate nanodevices such as carbon nanotubes and semiconductor nanowires exhibit properties that are difficult to achieve with conventional silicon microfabrication. Unfortunately, most such devices must be synthesized or processed in solution. To combine nanodevices into larger circuits, or simply to connect them with the macroscopic world, scientists use a range of directed self-assembly techniques to deposit them at specific locations on microfabricated chips. Many such methods work well with

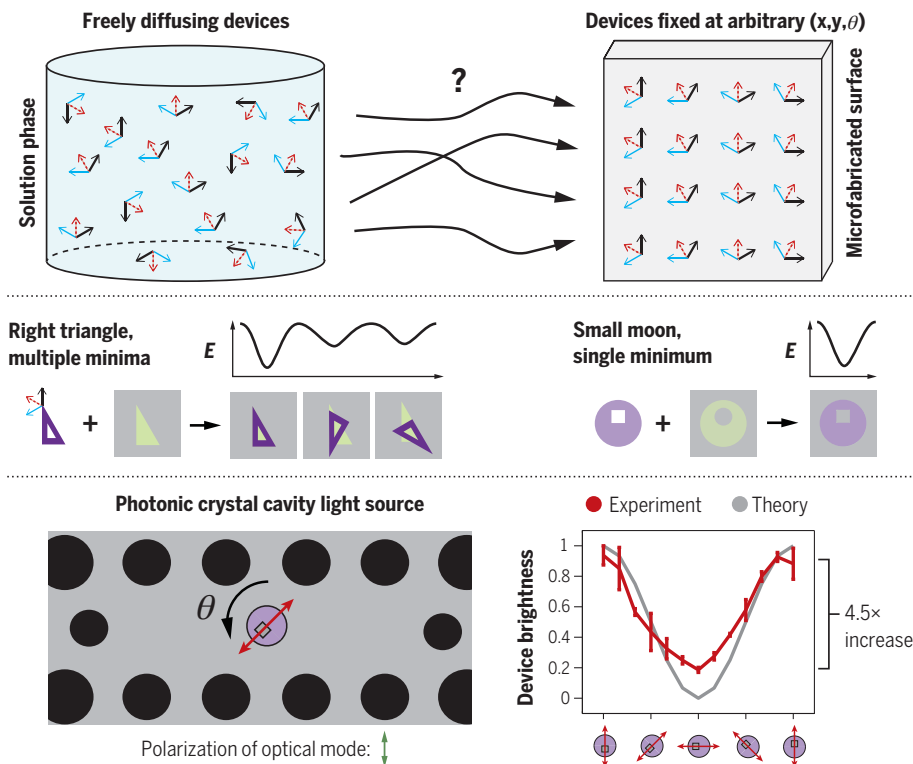
spherical devices for which orientation is irrelevant. For linear wire-like devices, flow or field alignment works for applications involving a single global orientation. However, a general solution for multiple orientations or less symmetric devices (e.g., diodes or transistors) has remained elusive.

**RATIONALE:** Single-molecule DNA origami shapes can simultaneously act as templates to create nanodevices and as adaptors to integrate them onto chips. With 200 attachment sites just

5 nm apart, origami can organize any material that can be linked to DNA; for example, carbon nanotube crosses have been templated to yield field-effect transistors. With ~100-nm outlines, origami are large enough that shape-matched binding sites can be written at arbitrary positions on chips using electron-beam lithography. Our prior work used equilateral triangles that stuck to binding sites in six degenerate orientations. Here, we asked whether origami shapes could provide both absolute orientation (to uniquely orient asymmetric devices) and arbitrary orientation (to independently orient each device). Success depended on finding a suitably asymmetric shape.

**RESULTS:** To break up-down symmetry and to ensure that each shape was deposited right-side up, we added adhesion-decreasing single-stranded DNAs to one side of each origami. The binding of asymmetric right triangles to shape-matched sites gave orientation distributions consistent with strong kinetic trapping, as predicted by the volumes of basins of attraction around local minima. This motivated the design of a “small moon” shape whose energy landscape has a single minimum. Fluorescent molecular dipoles fixed to small moons served as model nanodevices and allowed us to measure variability in orientation ( $\pm 3.2^\circ$ ) by polarization microscopy. Large-scale integration was demonstrated by an array of 3456 small moons in 12 orientations, which we used as a fluorescence polarimeter to indicate excitation polarization. The utility of orientation for optimizing device performance was shown by aligning fluorescent dipoles within microfabricated optical cavities, which showed a factor of 4.5 increase in emission.

**CONCLUSION:** Control over optical dipole orientation may enable metal nanorod metasurfaces at visible wavelengths, optimized coupling of emitters to nanoantennas, lumped nanocircuits, and coherence effects between small numbers of emitters. Still, these applications and the devices we present do not demonstrate the full power of the small moons: Dipolar devices can rotate  $180^\circ$  and still function. Completely asymmetric nanodevices requiring absolute orientation (e.g., molecular bipolar junction transistors) have yet to be developed; now that orientation can be controlled, there is motivation to invent them. In the meantime, the wiring of existing devices into circuits may be greatly simplified. ■



**Directed self-assembly of asymmetric DNA origami shapes enables orientation-controlled integration of chemically synthesized nanodevices with conventionally fabricated microdevices.**

Top: How can one transfer thousands of nanodevices to a surface and fix each with its own orientation independent of the others? Middle left: Naïvely, an asymmetric right triangle (dark purple) carrying a device could orient the device by sticking to a surface binding site (green) of the same shape. But such triangles often bind incorrectly because there are multiple minima in the energy landscape ( $E$ ). Middle right: The landscape for a disk with an offset hole (small moon, light purple) has a single minimum; thus, a small moon binds its site with a unique orientation. Bottom: The intensity of light emitted by a photonic crystal cavity microdevice (left) can be optimized (right) when small moons are used to align fluorescent molecule nanodevices (red arrow) with the polarization of the cavity mode.

The list of author affiliations is available in the full article online.

\*Corresponding author. Email: agopi@mit.edu (A.G.); pwkr@dna.caltech.edu (P.W.K.R.)

Cite this article as A. Gopinath et al., *Science* 371, eabd6179 (2021). DOI: 10.1126/science.abd6179

**S READ THE FULL ARTICLE AT**  
<https://doi.org/10.1126/science.abd6179>

## RESEARCH ARTICLE

## DNA ORIGAMI

## Absolute and arbitrary orientation of single-molecule shapes

Ashwin Gopinath<sup>1,2\*</sup>, Chris Thachuk<sup>3,4</sup>, Anya Mitskovets<sup>5</sup>, Harry A. Atwater<sup>5</sup>, David Kirkpatrick<sup>6</sup>, Paul W. K. Rothemund<sup>1,3,7\*</sup>

DNA origami is a modular platform for the combination of molecular and colloidal components to create optical, electronic, and biological devices. Integration of such nanoscale devices with microfabricated connectors and circuits is challenging: Large numbers of freely diffusing devices must be fixed at desired locations with desired alignment. We present a DNA origami molecule whose energy landscape on lithographic binding sites has a unique maximum. This property enabled device alignment within 3.2° on silica surfaces. Orientation was absolute (all degrees of freedom were specified) and arbitrary (the orientation of every molecule was independently specified). The use of orientation to optimize device performance was shown by aligning fluorescent emission dipoles within microfabricated optical cavities. Large-scale integration was demonstrated with an array of 3456 DNA origami with 12 distinct orientations that indicated the polarization of excitation light.

The sequential combination of solution-phase self-assembly (SPSA) and directed self-assembly (DSA) provides a general paradigm for the synthesis of nanoscale devices and their large-scale integration with control circuitry, microfluidics, or other conventionally fabricated structures. SPSA for the creation of sublithographic devices via structural DNA nanotechnology (1) is relatively mature. In particular, typical DNA origami (2) allow up to 200 nanoscale components, including carbon nanotubes (3), metal nanoparticles, fluorescent molecules, and quantum dots (4), to be simultaneously juxtaposed at 3 to 5 nm resolution within a 100 nm × 70 nm DNA rectangle. DSA uses topographic (5) or chemical (6–11) patterning, flow (12), or fields (13–15) to control the higher-order structure of molecules and particles. Although DSA is well developed for continuous block copolymer films (6), spherical nanoparticles (5), and linear nanostructures (10–14), it is less developed for origami-templated devices for which shape and symmetry play an important role in device function and integration.

Two challenges arise in DSA of origami-templated devices. The first is analogous to

the problem of absolute orientation (16) (Fig. 1A) in computational geometry: Given two Cartesian coordinate systems, what translation and rotation can transform the first to the second? Such transformations are key in computer vision and robotics, where they can be used to plan the motion of a virtual camera or a robot arm. For DSA, the analogous question arises: How can an asymmetric device in solution be positioned and aligned relative to a global laboratory reference frame? The second challenge is to achieve absolute orientation for many devices at once, such that the position and alignment of each device is arbitrary (i.e., independent of other devices) (Fig. 1B).

DNA origami placement (DOP) (9, 17) is a potential solution to both challenges. In DOP, the match between the overall shape of an origami and lithographically patterned binding sites is used both to position the origami in *x* and *y* and to control its in-plane rotation  $\theta$ . The strength of DOP is that thousands of origami can be oriented with high yield and fidelity: ~95% of sites have single origami aligned within  $\pm 10^\circ$  ( $\pm 1$  SD) of a desired value of  $\theta$ . The weakness of DOP has been the exclusive use of equilateral triangles, which can attach to their binding sites in one of six orientations (at any of three equivalent rotations, flipped right-side up or upside down). Thus, DOP of equilateral triangles does not achieve absolute orientation, and its use is limited to devices with compatible symmetry [e.g., pointlike (18), three-fold, or six-fold].

Consideration of fully asymmetric ( $C_1$  symmetric) devices, such as bipolar junction transistors, motivated the development of absolute and arbitrary DSA (Fig. 1C) and clarifies conditions for which DOP of high-symmetry

shapes (such as equilateral triangles and rectangles) or other DSA methods (fig. S1) are insufficient. If DOP of rectangular origami were used for the three-device circuit pictured, the origami's symmetry would allow it to bind in four orientations relative to each binding site: one (Fig. 1D) desired and three (Fig. 1, E to G) undesired. Random binding at each site would result in exponentially low yield: Only  $(0.25)^3 = 1.6\%$  of circuits would have all three transistors in the desired orientation.

Flow or field alignment of induced dipoles would allow the same four orientations. Field alignment of origami bearing fixed dipoles could break in-plane rotational symmetry but would still allow two orientations (Fig. 1, D and F) related by a horizontal flip. Further, such purely global methods cannot simultaneously specify distinct rotations or translations for multiple devices and could not fabricate the given circuit in a single step; arbitrary orientation promises independent alignment of an unlimited number of devices in a single step. Approaches that fix the ends of linear nanostructures on metal bars or dots (10, 11), or align them to chemical stripes (7), can add arbitrary control of position and in-plane rotation but still cannot distinguish among the orientations in Fig. 1, D to G. Nor can methods that fix the corners of rectangles (8).

We show that absolute orientation can be achieved by DOP with suitably asymmetric DNA origami shapes and demonstrate two applications in which absolute and arbitrary orientation work together to optimize or integrate optical devices. DOP could be performed on any planar substrate, such as silica, quartz, silicon nitride (SiN), and diamond-like carbon, and its surface could be differentiated into negatively charged binding sites (green features throughout this paper) that bound negatively charged DNA origami strongly in the presence of bridging  $Mg^{2+}$  ions, and a neutral background that bound origami weakly (shown as gray backgrounds). Here, binding sites patterned by electron-beam lithography (EBL) (19) were made negative with silanols that were ionized at the pH (8.3) of the origami binding buffer, and the neutral background was a trimethylsilyl monolayer generated through silanization.

DOP is a complex adsorption process that involves both three-dimensional (3D) diffusion to the surface and 2D diffusion of weakly bound origami on the background. Observations of lateral jamming, binding of multiple origami to a single site, and reorientation of origami already bound to sites suggested that DOP is both a nonequilibrium and a non-Langmuir process (17). Thus, to simplify development of absolute orientation, we separated the problem into two parts: (i) breaking up-down symmetry on unpatterned  $SiO_2$  (e.g., differentiating between the purple pair of

<sup>1</sup>Department of Bioengineering, California Institute of Technology, Pasadena, CA 91125, USA. <sup>2</sup>Department of Mechanical Engineering, Massachusetts Institute of Technology, Cambridge, MA 02139, USA. <sup>3</sup>Department of Computing and Mathematical Science, California Institute of Technology, Pasadena, CA 91125, USA. <sup>4</sup>Paul G. Allen School of Computer Science and Engineering, University of Washington, Seattle, WA 98195, USA. <sup>5</sup>Department of Applied Physics and Materials Science, California Institute of Technology, Pasadena, CA 91125, USA. <sup>6</sup>Department of Computer Science, University of British Columbia, Vancouver, British Columbia, Canada. <sup>7</sup>Computation and Neural Systems, California Institute of Technology, Pasadena, CA 91125, USA.

\*Corresponding author. Email: agopi@mit.edu (A.G.); pwkr@dna.caltech.edu (P.W.K.R.)

orientations in Fig. 1, D and E, and the orange pair in Fig. 1, F and G) and (ii) breaking rotational symmetry in the context of DOP (e.g., differentiating among the purple pair in Fig. 1, D and E).

### Breaking up-down symmetry

We explored the breaking of up-down symmetry using asymmetric right triangles (Fig. 2A). These triangles, synthesized via SPSA of 200

short DNA staple strands with a long scaffold strand, have left (orange) and right (purple) faces that were easily distinguished by atomic force microscopy (AFM) (Fig. 2A). Our idea

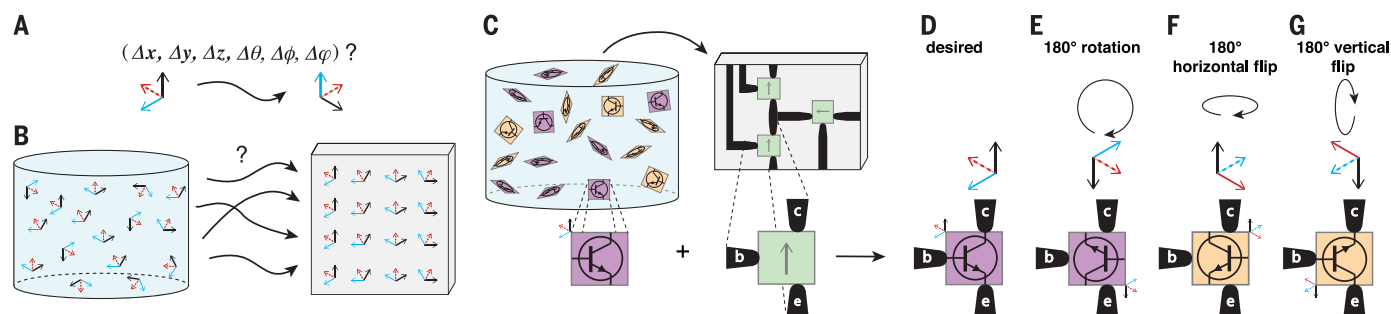


### Fig. 1. Challenges for directed self-assembly of origami-templated devices.

(A) The mathematical problem of absolute orientation. Bold arrows show in-plane axes; dashed arrows point into page; ordinary arrows point out. (B) The physical problem of absolutely orienting solution-phase (blue) devices on planar substrates (gray) so that each device has an arbitrary, user-specifiable orientation. (C) DNA origami placement (DOP) scheme for an asymmetric device (here, a bipolar junction transistor) shows the problem of using high-symmetry origami. Rectangles would

attach to binding sites (green) with four orientations (D to G), two right-side up (purple) and two upside down (orange). Electrodes c, e, and b can only connect to the transistor collector, emitter, and base, respectively, in a single (desired) orientation. Global methods are ruled out: Coordinate systems attached to origami indicate symmetries that prevent fields or flow from distinguishing among (D) to (G); the intended circuit contains three sites and two orientations (gray arrows) requiring arbitrary orientation.

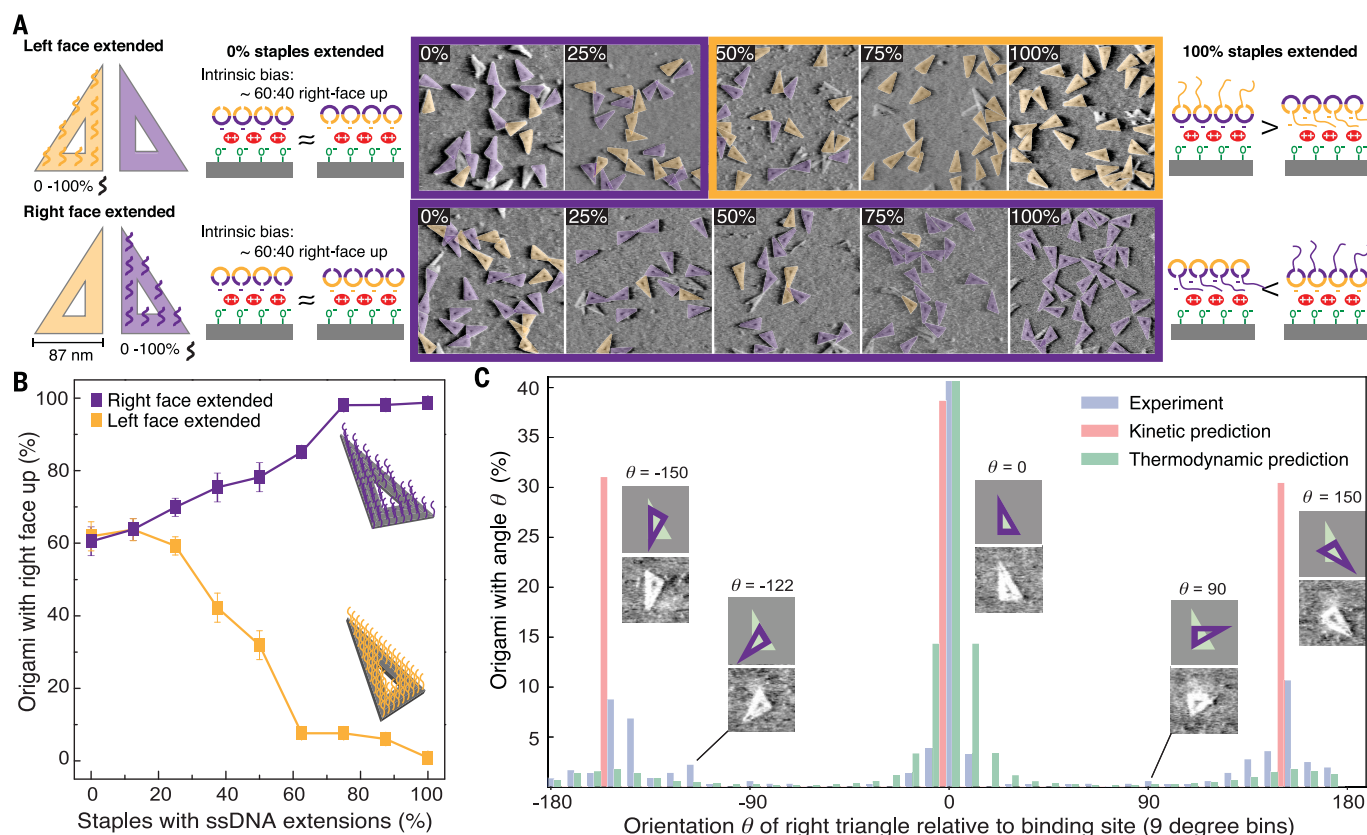


**Fig. 2. DOP of asymmetric right triangles.** (A) Before DOP, up-down symmetry was broken by extending staples on either the right face (purple) or left face (orange) with ssDNA [20 nt, poly(T)] at nicks in the phosphate backbone. From zero (0%) to 200 staples (100%) were extended. AFM shows that 100% extension caused nearly 100% bias on unpatterned SiO<sub>2</sub>, with extensions facing up; outline color reflects bias. Extensions interfere with binding of negatively charged phosphate groups to Mg<sup>2+</sup> ions (red)

immobilized on ionized silanols (green). (B) Summary of AFM data from (A). (C) AFM data (blue bars,  $N = 367$  sites) compared with kinetic (red) and thermodynamic (green) predictions for the percentage of right triangles bound at a given angle (within a 9° macrostate) on a shape-matched binding site. Insets show models of the highest-abundance microstate within a macrostate (purple triangles on green sites) and an AFM image of an example microstate.

was to make one side of the origami non-sticky and hence bias binding through the addition of single-stranded (ss) DNA extensions to the 5' ends of staples. To control for geometric details of the right triangle design, and to isolate intrinsic bias that might arise from these details instead of ssDNA extensions, we created two versions. In one version, the ends of all staple strands and hence all nicks in the phosphate backbone fell on the origami's right face; in the other, vice versa. Extensionless right triangles of both types, designed to be flat via twist correction (20), exhibited a weak preference to bind unpatterned SiO<sub>2</sub> with their right face up (~60:40 right:left, Fig. 2A); thus, intrinsic bias did not arise from asymmetric flexibility caused by nick position.

Bias has been observed in curved single-sheet structures elsewhere (21), which suggests that residual curvature caused by imperfect twist correction of the right triangle designs might be responsible for the observed bias. Strong bias (nearly 100%) was attained by adding 20-nucleotide (nt) poly(T) ssDNA extensions to the ends of all 200 staples; origami whose left face was extended bound left-face up, and vice versa (Fig. 1B). Adding poly(A) ssDNA to make all extensions double-stranded and rigid abolished the bias, supporting the idea that on SiO<sub>2</sub>, ssDNA extensions created bias by acting as entropic brushes that interfere with origami-SiO<sub>2</sub> binding: Floppy ssDNA extensions may incur a greater entropic penalty than do rigid dsDNA extensions when sandwiched between the origami and the surface. However, the symmetry-breaking effect of ssDNA extensions on SiO<sub>2</sub> did not generalize to other surfaces. On mica, where DNA-mica interactions are much stronger than DNA-SiO<sub>2</sub> interactions for the same Mg<sup>2+</sup> concentration (17), no bias was observed. On graphene, where  $\pi$ - $\pi$  interactions between the unpaired bases and graphene are attractive, the bias inverted.

### Breaking rotational symmetry

To break rotational symmetry, we began with the DOP of right-face extended triangles (Fig. 2C), used the results to develop a model of binding, and then used the model to design an origami shape that achieved absolute orientation. AFM images of sites binding a single right triangle (61% of  $N = 600$  sites; fig. S2) were analyzed, and the angle  $\theta$  between origami and binding site was measured to the nearest multiple of 0.5°. Only 40% of origami bound with the desired alignment ( $\theta = 0^\circ, 9^\circ$  wide macrostate), too few for reliable absolute orientation. Major peaks for undesired orientations were observed at  $\theta = -150^\circ$  (8.7%) and  $150^\circ$  (10.6%). Similar results were obtained for DOP of left-face extended triangles (figs. S3 and S4). We next considered whether the distribution of states better fit a kinetic or

equilibrium model, under the assumption that the binding energy of a given state is linearly proportional to the area of overlap between the origami and binding site;  $\theta = 0^\circ$ , with its total overlap of origami and binding site, has the highest possible binding energy. The state space was discretized in both  $x$  and  $y$  (1-nm increments) as well as  $\theta$  (1° increments), encompassing more than 19 million states with positive overlap.

For thermodynamic predictions (Fig. 2C, green), we calculated expected equilibrium abundances from the partition function, using an energy per unit area overlap derived by constraining the abundance at the  $\theta = 0 \pm 4^\circ$  macrostate to match the experiment (Fig. 2C, blue). Except where constrained to match experiment, thermodynamic abundances underestimated peak experimental abundances by large factors (e.g., from 5.1 $\times$  for  $\theta = -150^\circ$  to 5.9 $\times$  for  $150^\circ$ ). Thermodynamic abundances failed to predict minority states at  $\theta = -122^\circ$  or  $90^\circ$ . Calculations using smaller macrostates (3° or 1°) gave larger discrepancies. For kinetic predictions (Fig. 2C, red), we performed steepest-ascent hill climbing using all possible states as initial configurations, and found (neglecting variations in  $x$  and  $y$ ) that the state space had three basins of attraction whose maxima ( $\theta = 0^\circ, -150^\circ, 150^\circ$ ) corresponded to the three most common experimental states. Kinetic abundances predicted by measuring and normalizing basin volumes closely matched the experimental abundance at  $\theta = 0^\circ$  (0.95 $\times$ ) without constraint, and matched better than thermodynamic predictions for  $\theta = -150^\circ$  (3.6 $\times$ ) and  $150^\circ$  (2.9 $\times$ ). Small changes to details of the kinetic model (fig. S5, A and B) predicted the existence but not the quantitative abundance of minority states (e.g.,  $\theta = -122^\circ$  or  $90^\circ$ ). Thus, our data were most consistent with a strongly kinetically trapped regime in which origami entered the state space at random (when they collide with a binding site) and simply proceeded to a local maximum (fig. S6A) in binding energy.

The strong kinetic trapping exhibited by DOP constrains the energy landscapes that can robustly break rotational symmetry: The volume of a single basin of attraction must comprise most of the state space. In the best case, the landscape would have a unique global maximum. Exact analysis (22) and general yet simple geometric arguments (23) have shown the existence of a unique global maximum for a disk with an offset hole (Fig. 3A), a shape we call a "small moon." Experiments with millimeter-scale models on hydrophobic binding sites (24) confirmed that small moons translate and rotate to a unique orientation from initial configurations created by hand using tweezers. Here, we approximated the small moon shape by a DNA origami (Fig. 3B and fig. S7A) with

an offset square hole (circumscribed by the ideal hole).

To predict the performance of the approximate small moon, we began by analyzing the discretized energy landscape of a circle with a square hole; it had a unique global maximum in its energy landscape, although the hole slightly flattened the landscape in some regions (compare Fig. 3C with Fig. 3D and fig. S6, B and C). However, the exact jagged outline and aspect ratio of the DNA origami small moon (fig. S7A) gives more complex results depending on the inner and outer diameters of the circles of its cognate binding site: For a wide range of diameters, more than 90% of origami bind within a single degree of the correct orientation (fig. S8, blue histograms), but for some diameters, a few percent of origami get trapped in maxima that are rotated  $\sim 180^\circ$  from the correct orientation (fig. S8, blue and red histograms); for other diameters, no origami are flipped but the quality of orientation is not as high (fig. S8, black histograms). DOP of small moon origami with ssDNA extensions to break up-down symmetry (fig. S7D) was performed on both disk-shaped control sites (Fig. 3E and fig. S9) and shape-matched sites (Fig. 3F and fig. S10). The average of 498 AFM images of control sites with single origami (83% of 600 total sites) gave an annular shape indicating random orientation; the average of 592 images on shape-matched sites (98.7% of 600 total sites) reconstructed the small moon shape, confirming unique alignment.

### Orientation of fluorescent dipoles

By fitting the small moon shape to AFM of small moon origami on shape-matched sites, we found that alignment varied by  $\pm 6.7^\circ$  ( $\pm 1$  SD). This variability included real variabilities caused by fabrication error or imperfect assembly, as well as spurious variability caused by the fitting of a model shape to poorly resolved origami; the latter error was difficult to estimate. To get a better estimate of alignment precision, we imaged small moons intercalated post-DOP with the fluorescent dye TOTO-3 (Fig. 3, G to J, and figs. S11 and 12). For 600-site arrays of small moons on disk-shaped control and shape-matched sites, we measured emission intensity for excitation polarization  $\beta$  in 10° steps (sampling each  $\beta$  twice by rotating the stage from 0° to 350°) and fit the emission to derive distributions for the origami orientation  $\beta$ . The reported angle between the molecular absorption dipole of TOTO-3 analogs and the DNA helix axis ( $\phi$ ) ranged from 61° to 90° (25–28), but the exact angle was unimportant for measuring variability: It was close enough to 90° that averaging over multiple dyes (intercalated at varying rotations as caused by twist; Fig. 3B) resulted in a strongly anisotropic net dipole strength in the plane of the origami.

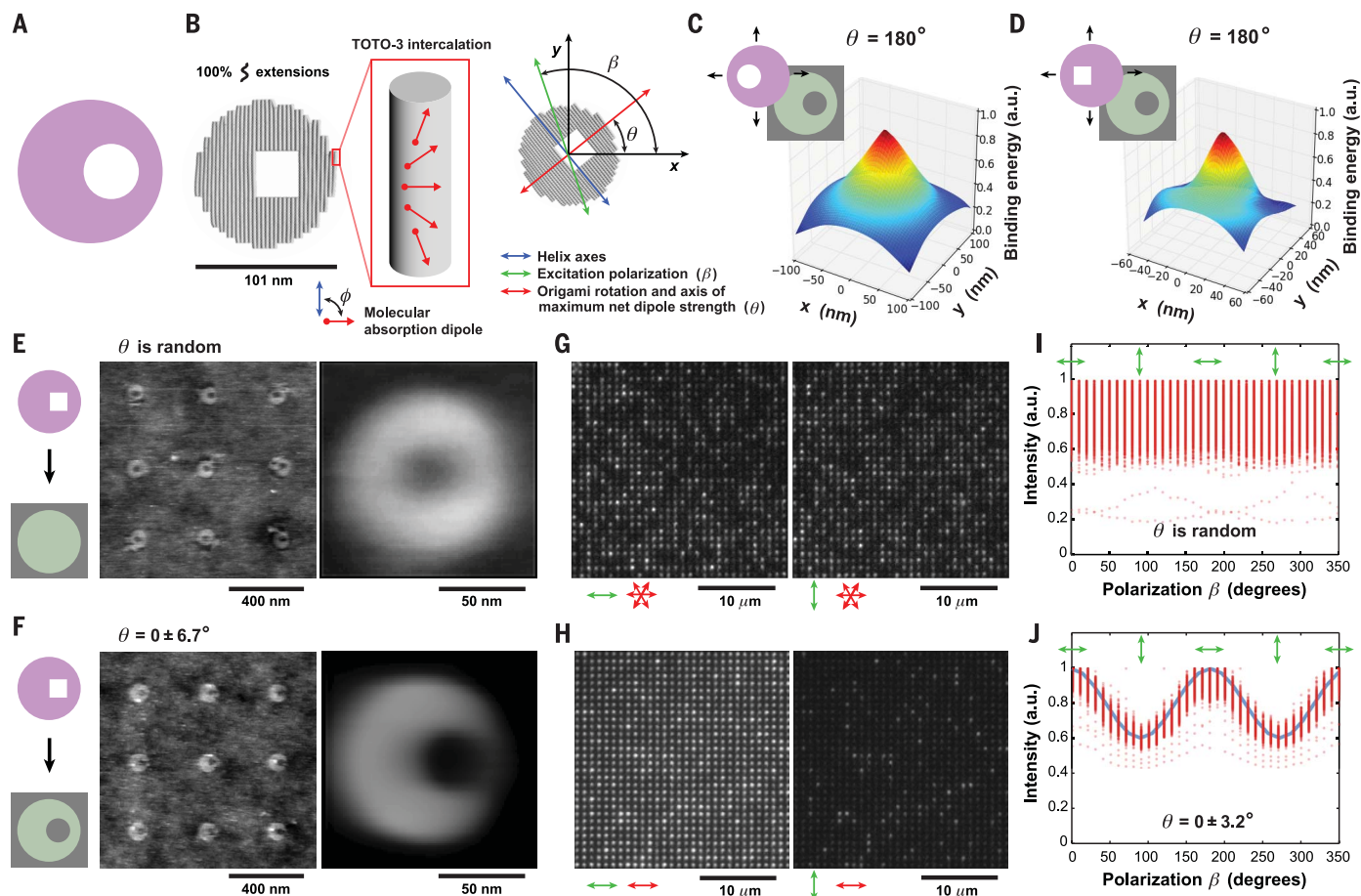


**Fig. 3. Breaking rotational symmetry.** (A) Ideal ring with offset hole. (B) DNA origami approximation of (A) comprising 34 parallel helix axes (gray cylinders). Inset shows rotation of the fluorescent dye TOTO-3's absorption dipole along the length of a TOTO-3 intercalated helix. Coordinate system shows relations among helix axes, excitation polarization ( $\beta$ ), and origami rotation ( $\theta$ ). (C) Section of energy landscape for ideal shape (A) on binding site,  $\theta = 180^\circ$ . Colors run from high

binding energy (red) to low (blue). (D) Same as (C), for experimental shape (B). (E and F) AFM and averaged AFM ( $N = 600$ ) of DOP on arrays of disk-shaped and shape-matched sites. (G and H) Fluorescence microscopy of TOTO-3 intercalated into DOP arrays on disk-shaped and shape-matched sites (excitation 642 nm; emission 660 nm). (I and J) Intensity (red dots) of  $N = 600$  sites in (G) and (H) as a function of excitation polarization  $\beta$ . Blue line denotes the best fit.

Emission peaked for  $\beta$  perpendicular to the helix axes (28), coincident with  $\theta$ . The strength of a molecular dipole  $\mu$  excited by an electric field  $\mathbf{E}$  along the direction of unit vector  $\hat{\mathbf{e}} = \mathbf{E}/|\mathbf{E}|$  is  $D(\mathbf{E}) = |\mu \cdot \hat{\mathbf{e}}|^2 = |\mu|^2 \cos^2(\beta - \theta)$ , where  $\beta$  is the polarization of  $\mathbf{E}$  and  $\theta$  is the in-plane dipole angle. According to the dipole approximation (29, 30), emission is proportional to absorption, which is proportional to  $|\mathbf{E}|^2 D(\mathbf{E})$ . The experimental intensity could be fit to  $I_0 \cos^2(\beta - \theta) + c$ , where  $I_0$  is the maximum emission and  $c$  is the background (camera noise and reflection). Emission from a collection of  $n$  molecular dipoles  $\mu_k$  bound to an origami was proportional to  $|\mathbf{E}|^2 D_{\text{net}}(\mathbf{E})$ , where the net dipole strength (31) is given by  $D_{\text{net}}(\mathbf{E}) = \sum_{k=1}^n |\mu_k \cdot \hat{\mathbf{e}}|^2$ .

Thus, the experimental intensity of  $n$  molecular dipoles with an anisotropic net in-plane dipole strength could be fit to the  $\cos^2$  expression above: If  $\mathbf{E}_{\parallel}$  and  $\theta$  are defined to

lie along the direction of maximum net dipole strength, then  $I_0$  is proportional to the difference  $D_{\text{net}}(\mathbf{E}_{\parallel}) - D_{\text{net}}(\mathbf{E}_{\perp})$  and  $c$  is the background plus a contribution proportional to  $D_{\text{net}}(\mathbf{E}_{\perp})$  from the direction of smallest net dipole strength. Emission from control sites (Fig. 3I and fig. S13, A and B) individually fit this expression, but individual values of  $\theta$  were uniformly distributed (fig. S13C), both confirming random origami orientation and ruling out polarization anisotropy in our setup. As expected, aggregate data could not be fit. In contrast, aggregate data for shape-matched sites (Fig. 3J) fit  $\theta = 0^\circ$ , and fits to individual sites (fig. S13D) varied by  $\pm 3.2^\circ$  ( $\pm 1$  SD), our best estimate of alignment precision.

#### Large-scale integration

TOTO-3 intercalation of small moons further enabled us to demonstrate arbitrary orientation, prototype the large-scale integration of

orientation-dependent devices, and explore variables that could affect the quality of polarization-based devices. An important parameter for such orientation-dependent devices is the bleed-through of emission signal from orthogonal polarization channels. We quantified bleed-through for the data in Fig. 3J; after background subtraction, we found that emission from origami perpendicular to  $\beta$  was 30% of that from origami parallel to  $\beta$ . In interpreting the source of bleed-through, we considered only the effect of dye alignment and neglected small polarization mixing effects of high numerical aperture on excitation polarization (29). In an ideal device, all dye molecules would align perfectly with  $\mathbf{E}_{\parallel}$ ;  $D_{\text{net}}(\mathbf{E}_{\perp})$  and hence bleed-through would be zero.  $D_{\text{net}}(\mathbf{E}_{\perp})$  combines contributions from both placement variability in  $\theta$  with incoherence of dye angle relative to the origami. The contribution from placement variability

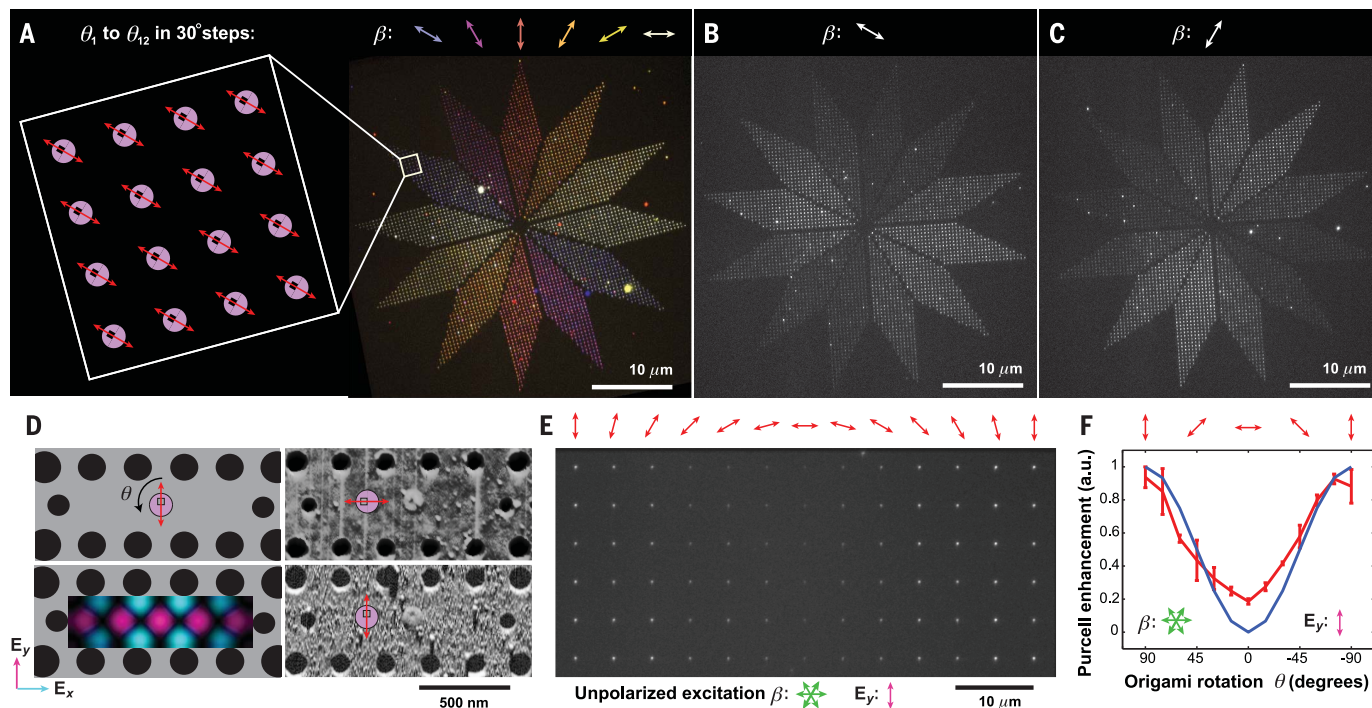


**Fig. 4. Applications of orientation.** (A) 2D polarimeter composed of 3456 origami divided into 12 rhomboidal arrays, with  $\theta$  graduated in  $30^\circ$  steps. (B and C) Fluorescence images of the polarimeter at two different polarizations; for all polarizations, see fig. S15. (D) Schema, simulation, and AFM for coupling between TOTO-3 emitters and PCCs as a function of origami rotation  $\theta$ .  $E_y$

(purple) and  $E_x$  (blue) label polarization for FDTD simulation (8) of the electric field. Red axes show polarization of peak TOTO-3 emission. (E) Fluorescence of a PCC array with varying  $\theta$ , excited by unpolarized light  $\beta$ . Maximum coupling is observed when origami align TOTO-3 emission dipoles with  $E_y$ . (F) Data (red) from (E) and simulation (blue). Error bars,  $\pm 1$  SD;  $N = 6$ .

was small, as bleed-through would be only 0.3% were the  $\pm 3.2^\circ$  variability the only source;  $\pm 39^\circ$  variability would be required to explain 30% bleed-through.

The contribution from incoherent dye alignment within an origami is itself complex: It combines the deterministic rotation of  $\phi$  by DNA twist, random wobble (32, 33) from rotational diffusion (reduced here by intercalation and drying), potential alternative binding modes (34), and substantial ( $\sim 10.6^\circ$ , fig. S14) back-and-forth bending of each helix axis in a DNA origami (2). Here we explain bleed-through simply by a combination of  $\phi$  and helix bending, which are the most relevant variables for devices based on intercalators. Attributing all bleed-through to the dipole-helix angle yielded  $\phi = 69^\circ$ , and adding helix bending increased our estimate of  $\phi$  to  $70^\circ$ ; both values are consistent with  $\phi$  previously measured for TOTO-3 analogs. As with the addition of helix bending, adding other sources of dye alignment incoherence or excitation polarization mixing to the model would increase our estimate of  $\phi$ ; thus, given our data,  $69^\circ$  was a lower bound for  $\phi$ . However, even if  $\phi = 90^\circ$  were achieved and all other sources of alignment incoherence were removed, helix bending would still cause  $\sim 3.5\%$  bleed-through, an unavoidable consequence of randomly intercalating dyes binding to both  $+10.6^\circ$  and  $-10.6^\circ$  bent helices. Devices with

better-defined alignment relative to DNA origami, such as gold rods (35) or single site-specific rigidly linked chromophores (36), would exhibit much stronger polarization effects, limited only by the placement variability (i.e., 0.3% bleed-through might be attained).

Despite the limitations of intercalating dyes, Fig. 4, A to C, shows that arbitrary orientation could integrate 3456 TOTO-3-labeled small moons with 12 different  $\theta$  values into a microscopic fluorescent polarimeter, a  $100\text{-}\mu\text{m}$  device that glows most strongly along the polarization axis of incident light. Microscopic polarimeters constructed with plasmonic antennas have been created in the near-infrared (near-IR) (37), and arrays of oriented gold rods have been used for metasurface polarimeters at telecommunication wavelengths (38). Such on-chip instruments could replace multiple bulky and expensive optical components and would enable in situ measurements within devices or transmission lines. Because our polarimeter reports polarization directly, it could be fabricated on microscope slides and used in situ to aid polarized fluorescence microscopy (39); specifically, it could be used to align excitation polarization grossly by eye without requiring analyzers, to check for polarization bias, or as a calibration standard for fluorescence anisotropy of biomolecules.

The operating wavelength could be tuned by intercalation of different dyes (e.g., YOYO-1, 491 nm excitation; TOTO-1, 514 nm; YOYO-3, 612 nm; TOTO-3, 642 nm) or made broadband by using a mixture.

On the basis of the  $\pm 3.2^\circ$  variability we observed, fitting the orientation of 3456 origami would allow the angle between excitation polarization and surface features to be measured with a precision of  $0.05^\circ$  (standard error of the mean). Our polarimeter was unable to measure  $z$ -polarization, but DOP of 3D origami could add this capability. Although our polarimeter was not a metasurface, it provides a roadmap for how DOP could push metal-rod metasurfaces from the near-IR, where the rods are fabricated lithographically, to the visible, by means of oriented arrays of smaller colloidal gold rods (35).

#### Optimizing device performance

The variability in orientation demonstrated here, together with the previously demonstrated (18) positional variability [ $\pm 28$  nm ( $\pm 1$  SD)], may render origami placement insufficient for the construction of nanoelectronics devices with single-nanometer critical distances, but placement is particularly appropriate for the construction of optical nanodevices where its precision and accuracy are sufficient to observe subwavelength effects. Hybrid nanophotonic

devices (40) combine light emitters or scatterers with microfabricated optical resonators to obtain devices as various as biosensors (41) and light sources for on-chip quantum information processing (42). The performance (e.g., sensitivity of a detector, or intensity of a light source) of such devices hinges on the strength of the coupling between the emitter and resonator. In particular, emission intensity is proportional to the cavity Purcell enhancement  $F_{\text{cav}} \propto |\boldsymbol{\mu} \cdot \mathbf{E}(\mathbf{r})|^2$ , which is typically a sensitive function of the position of the emitter  $\mathbf{r}$  and the orientation of the emission dipole  $\boldsymbol{\mu}$  relative to the cavity electric field  $\mathbf{E}$  (43). To maximize coupling, the emitter should be positioned in a peak of a resonant mode, with  $\boldsymbol{\mu}$  aligned to the polarization of  $\mathbf{E}$  at  $\mathbf{r}$ . Fabrication of resonators with simultaneously positioned and aligned emitters has been a difficult challenge (44).

Most approaches for positioning involve randomly growing or depositing emitters on a surface, selecting emitters by microscopy, and tediously fabricating resonators around them (42, 43). Some emitters can be grown at predetermined sites within resonators (45), but in general, deterministic approaches for positioning emitters rely on scanning probe microscopy (46, 47). Neither select-and-postprocess nor scanning probe approaches can scale to large numbers of devices, or provide deterministic alignment. Conversely, methods for achieving deterministic alignment of molecular or vacancy-based emitters (48–50) do not address positioning. Previously (18), we used DOP to achieve the large-scale positioning of molecular emitters within L3 photonic crystal cavities (PCCs); TOTO-3 intercalated small moons allowed us to extend that work to control the alignment  $\theta$  of  $\boldsymbol{\mu}$  in the cavity (Fig. 4, D to F). To optimize emission from the PCCs, we created a 13×6 array of identical resonators (figs. S16 and S17) with small moons positioned in the center of a  $y$ -polarized peak in  $\mathbf{E}$ , and varied  $\theta$  in 13 steps from 90° to –90° across the width of the array.

Emission intensity roughly followed the expected  $\cos^2(\theta)$  relationship, and a factor of 4.5 increase was observed for the  $\theta$  value that maximally aligned TOTO-3 dipoles with  $\mathbf{E}_y$ . Potential reasons for disagreement between experimental intensity at 0° with finite difference time domain (FDTD) simulation of a single dipole are similar to those for bleed-through above: TOTO-3 dyes could be spread out over the 100-nm-diameter disk of the small moons rather than in the exact center of the cavity,  $\phi \neq 90$  could contribute to a net dipole strength parallel to  $\mathbf{E}_z$ , and alignment error could occur. Beyond emitter-in-cavity devices, our ability to simultaneously position and orient molecular and nanoparticle components should find wide use in nanophotonics. The collective behavior of multiple

emitter systems is highly sensitive to inter-emitter distance and relative dipole orientation, which implies that our technique will be ideal for studying and engineering fundamental phenomena such as superradiance (51) and other coherence effects (52). Positioning and orientation of molecular emitters within optical nanoantennas would allow antenna performance to be optimized (53); similar control over metal nanoparticle dipoles would enable optical nanocircuit elements to be programmed with series, parallel, or intermediate behavior (54).

## Discussion

We have engineered the energy landscape of DNA origami shapes on binding sites to realize absolute and arbitrary orientation, enabling DSA to independently specify all degrees of freedom and thus break all translational and rotational symmetries for arbitrary numbers of  $C_1$ -symmetric molecular devices. Perhaps surprisingly, we achieved this by combining broken up-down symmetry with a mirror symmetric ( $D_1$ , bilateral) shape: the small moon. [A fully asymmetric ( $C_1$ ) shape was neither necessary nor sufficient; the  $C_1$ -symmetric right triangle suffered from kinetic trapping (55, 56).] Yet the devices we have presented did not demonstrate the full power of the small moons; the twofold degeneracy of transition dipoles means that  $D_2$  symmetric shapes (e.g., an elongate rectangle or oval) could have been used.

No isolated optical device, nor any coupled array of optical devices, designed to date seem to require full symmetry-breaking: 2D chiral scatterers (57) ( $C_4$ ) require up-down symmetry to be broken, but not rotational symmetry; U-shaped resonators ( $D_1$ ) for certain nonlinear metasurface holograms (58) require that complete rotational symmetry be broken but not up-down. Within electronics, no molecular device with the  $C_1$  symmetry of a bipolar junction transistor has been achieved: Molecular diodes (59) ( $D_1$ ) can tolerate flips about their mirror plane, and crossed-carbon nanotube field-effect transistors (3) ( $D_2$ ) can tolerate two flips and 180° rotation. On the other hand, proposed planar optical and electronic circuits (60) of even just a few symmetric components can almost invariably take advantage of absolute and arbitrary orientation to avoid tortuous paths for interconnect. In part, applications for DSA of molecular components have been constrained by what has been possible. Now that molecular orientation can be controlled, we anticipate that new asymmetric devices and architectures will be explored.

## Materials and methods

### Origami design

Origami were designed with caDNAno (61) so that single-stranded 20-T polythymidine exten-

sions to 5' staple ends would all project from the same face of the origami. Staple strands (Integrated DNA Technologies, 100  $\mu\text{M}$  each in water) and the scaffold strand (single-stranded M13mp18 from Bayou Biolabs for right triangles; p8064 from Tilibit for small moons) were mixed together to target concentrations of 100 nM (each staple) and 40 nM, respectively (a 2.5:1 staple:scaffold ratio) in 10 mM Tris Base, 1 mM EDTA buffer (adjusted to pH 8.35 with HCl; acetic acid was avoided to prevent high background in AFM) with 12.5 mM magnesium chloride. We heated 50- $\mu\text{l}$  volumes of staple/scaffold mixture to 90°C for 5 min and annealed them from 90° to 20°C at –0.2°C/min in a PCR machine. We used 0.5-ml DNA LoBind tubes (Eppendorf) to minimize loss of origami to the sides of the tube.

A high concentration of excess staples prevents origami placement. Thus, origami were purified away from excess staples using 100-kD molecular weight cutoff spin filters (Millipore). To maintain consistency for each series of experiments, a single high-concentration stock solution (15 to 20 nM origami) from a single purification was maintained for each shape and was diluted to a nominal concentration of 100 pM immediately before use.

### Fabrication of binding sites and PCC arrays

Fabrication of binding sites was similar to that described in (17, 18). For non-PCC experiments, fabrication began with a thermally grown  $\text{SiO}_2$  layer (on a silicon wafer), which was cleaned and passivated via vapor deposition of HMDS (hexamethyldisilazane). A thin (80 nm) layer of PMMA 950 A2 (MicroChem) was spin-coated on the substrate as a resist. After binding sites were defined via EBL, they were activated via selective removal of the passivation layer using an anisotropic  $\text{O}_2$ -plasma etch. Finally, the residual PMMA resist was removed to reveal a substrate that was composed of two chemically distinct regions: (i) origami-shaped features covered with ionizable surface silanols (–OH) and (ii) a neutrally-charged background covered with trimethylsilyl groups. This procedure enabled good placement in 35 mM  $\text{Mg}^{2+}$ . For PCC experiments on silicon nitride, the complex geometry of the holes and membranes prevented the passivation of some surfaces. To avoid nonspecific binding to these surfaces, we performed DOP at a lower  $\text{Mg}^{2+}$  concentration of 12.5 mM. To achieve strong adhesion to binding sites under this condition, we silanized activated sites with 0.1% carboxyethylsilanetriol (CTES, Gelest) before the resist was stripped.

Fabrication of PCC arrays was similar to that described (18) for “isolated PCCs,” rather than the process for “close-packed arrays,” because the small PCC arrays described do not justify the more complex process used to fabricate large suspended arrays of PCCs. A

schematic of the fabrication process is shown in fig. S16 and SEM of the result in fig. S17. Fabrication began with double-side polished silicon wafers (University Wafers or Rogue Valley Microdevices) with 275-nm layers of LPCVD-grown SiN on both sides. Each wafer was cleaned and alignment markers were defined in the SiN layer by EBL and modified-Bosch ICP etching. The substrate was then cleaned and passivated as above. Next, binding sites were defined using EBL using the previously defined alignment markers, activated, and CTES-silanized. After resist stripping, new resist was spun on, and PCCs were defined around binding sites by EBL and modified-Bosch ICP etching of the SiN layer. Finally, PCCs were suspended using a XeF<sub>2</sub> isotropic etch of the underlying silicon.

### FDTD simulations of PCCs

Three-dimensional FDTD simulation (FDTD Solutions, Lumerical) was used both for PCC design and to generate simulated LDOS for comparison with experimental maps of the resonant cavity modes. To design the photonic crystal, we fixed the refractive index of SiN at 2.05, the thickness of the SiN membrane at 275 nm, and adjusted  $r$ ,  $r/a$ ,  $r_1$ ,  $r_2$ , and  $s$  (fig. S17A, inset) to maximize quality factor within the wavelength range of 655 to 660 nm. Photonic crystal size was set to  $20a$  in the  $x$  direction and  $34.64a$  in the  $y$  direction. Boundary conditions were implemented by introducing a perfect matching layer around the structure. The simulation discretization was set to  $a/R$  in the  $x$ -direction,  $0.866a/R$  in the  $y$ -direction, and  $a/R$  in the  $z$ -direction, where the variable  $R$  was set to 10 for PCC design (so that PCC parameter could be quickly optimized), and set to 20 to generate simulated LDOS of higher resolution for comparison with experimental mode maps. The simulation modeled emission from a single dipole with polarization  $P(x, y, z) = (1, 1, 0)$ , located at a weak symmetry point close to the cavity surface.

### Origami placement experiments

DOP proceeded in four steps: binding, a series of initial washes, a series of surfactant washes, and a series of final washes. See troubleshooting guide in the supplementary materials for an enumeration of problems and suggestions, and previous work (17) for images of substrates during the placement process.

For binding, a 50-mm petri dish was prepared with a moistened lint-free wipe to limit evaporation. For non-PCC samples, solution with 100 pM origami was prepared in “placement buffer” (10 mM Tris, 35 mM Mg<sup>2+</sup>, pH 8.3). A 20- $\mu$ l drop was deposited in the middle of the chip and incubated for 1 hour. For PCC arrays, 12.5 mM Mg<sup>2+</sup> was used instead. After incubation, excess solution-phase origami were removed with at least 8 buffer washes, each

performed by pipetting 60  $\mu$ l of fresh placement buffer on and off the chip two to three times. Next, to remove origami that were non-specifically bound to the passivated background, the chip was buffer-washed five times using 20 to 40  $\mu$ l of “Tween washing buffer” (placement buffer with 0.1% Tween 20 surfactant) and left to incubate for 30 min. Lastly, the chip was buffer-washed 8 times back into either a higher pH “stabilizing buffer” for wet AFM imaging (10 mM Tris, 35 mM Mg<sup>2+</sup>, pH 8.9; this prevented movement during AFM) or placement buffer for subsequent drying. These final high-volume washes (60  $\mu$ l) were performed to completely remove Tween 20. After the last wash, the chip was left with roughly 20  $\mu$ l of buffer and was ready for AFM imaging or drying. Binding sites were prevented from drying at any point during binding or subsequent washes to avoid dewetting artifacts.

### AFM characterization

AFM images were acquired using a Dimension Icon AFM (Bruker) using the “short and fat” cantilever from a “sharp nitride lever” probe (SNL, 2 nm tip radius, Bruker). Non-PCC samples were imaged in fluid tapping mode, using a cantilever resonance between 8 and 10 kHz. Phase imaging was used to achieve high contrast while minimizing tip-sample interaction. PCC samples were imaged in air in contact mode. AFM images were processed using Gwyddion. Single and multiple binding events for placed origami were hand-annotated and measurements of right triangle and small moon orientation were made by hand, aided by Matlab scripts. For example, in the case of right triangles, an overlay of a green reference image on top of a red test image was used to allow a user to translate and rotate (in 0.5° steps) the reference image relative to the test image, until a maximum overlap was achieved. The script automatically recorded  $x$ ,  $y$ , and  $\theta$  for that test image and presented the next test image. To prevent user bias, the orientation of the reference image was randomized for each test image, and the orientation of the reference image was obscured from the script user.

### Optical experiments

For fluorescence experiments, surface-bound origami were incubated in placement buffer containing 1 nM TOTO-3 (Invitrogen; Thermo-Fisher) for 10 min at room temperature and dried via ethanol drying: 10 s in 50% ethanol, 30 s in 75% ethanol, and 120 s in 90% ethanol. Remaining ethanol was removed by air drying.

Imaging was performed with an Olympus BX-61 microscope with a xenon excitation source and Hamamatsu EMCCD cooled to -75°C. For fluorescence imaging of non-PCC samples, excitation light was filtered with a 640-nm shortpass filter and emission light

was longpass-filtered via a 645-nm dichroic. For the PCC array, an additional  $655 \pm 5$  nm bandpass filter was used to select the PCC's fundamental wavelength of 657.2 nm. For non-PCC samples, excitation light was filtered with an additional linear polarizer, mounted on a rotatable adaptor to allow selection of the desired excitation polarization  $\beta$  relative to the sample axis. For non-PCC samples, fluorescence emission was collected using a 50 $\times$  objective (1.0 NA oil, optimized for polarized light, samples were simply immersed in oil without coverglass); for the PCC array, a 50 $\times$  (0.8 NA air) objective was used.

Photoexposure was limited to prevent photobleaching. For both PCC and non-PCC samples, complete bleaching took ~45 s under constant illumination; exposure was limited to less than 10% of this time. For non-PCC samples, the integration time for each polarization angle was 100 ms, yielding 3.6 s of total for orientation measurements, and 1.2 s for the polarimeter. The final image of the PCC array (Fig. 4E) was created by averaging images from three separate samples, each imaged with an integration time of 1 s.

### Kinetic and thermodynamic predictions

For kinetic predictions, shapes were assumed to land randomly in the energy landscape when they first bind a site. To find the distribution of final states, we used steepest-ascent hill climbing starting from all possible nonzero-energy initial configurations  $(x, y, \theta)$  of a shape on its binding site. From a particular configuration, the neighboring configuration that most improved the energy (area of overlap) was selected as the new state, and simulation ended when no neighbor could improve upon the current state. The distribution of final states was sensitive to the choice of neighborhood, as determined by the types of allowable moves. Thus, we explored simulations (fig. S5) in which a single move was limited (i) to independent  $x$ ,  $y$ , or  $\theta$  movement, (ii) to potentially simultaneous  $x$  and  $y$  movement and independent  $\theta$  movement, and (iii) to potentially simultaneous  $x$ ,  $y$ , and  $\theta$  movement.

For thermodynamic predictions, a partition function was constructed using again the area of overlap as the energy. All possible nonzero energy configurations  $(x, y, \theta)$  served as microstates, and macrostates of interest were constructed by collapsing all microstates of a particular  $\theta$  into a single state. Energy per unit area overlap ( $E_{\text{overlap}}$ ) occurred as a free parameter in this partition function. Thus, we computed a plausible probability distribution for angle-based macrostates in two stages. First, for a given angular bin size ( $\Delta\theta = 1^\circ, 3^\circ$ , or  $9^\circ$ ), binary search was performed on  $E_{\text{overlap}}$  until the theoretical probability of the most abundant macrostate ( $\theta = 0^\circ$ ) matched the

experimental probability within  $\epsilon = 10^{-7}$ . Second, using the resulting  $E_{\text{overlap}}$  and the partition function, probabilities were calculated for all macrostates for  $-180^\circ \leq \theta < 180^\circ$ .

## REFERENCES AND NOTES

- N. C. Seeman, DNA in a material world. *Nature* **421**, 427–431 (2003). doi: [10.1038/nature04046](https://doi.org/10.1038/nature04046); pmid: [12540916](https://pubmed.ncbi.nlm.nih.gov/12540916/)
- P. W. K. Rothmund, Folding DNA to create nanoscale shapes and patterns. *Nature* **440**, 297–302 (2006). doi: [10.1038/nature04586](https://doi.org/10.1038/nature04586); pmid: [16541064](https://pubmed.ncbi.nlm.nih.gov/16541064/)
- H. T. Maune *et al.*, Self-assembly of carbon nanotubes into two-dimensional geometries using DNA origami templates. *Nat. Nanotechnol.* **5**, 61–66 (2010). doi: [10.1038/nnano.2009.311](https://doi.org/10.1038/nnano.2009.311); pmid: [19898497](https://pubmed.ncbi.nlm.nih.gov/19898497/)
- R. Schreiber *et al.*, Hierarchical assembly of metal nanoparticles, quantum dots and organic dyes using DNA origami scaffolds. *Nat. Nanotechnol.* **9**, 74–78 (2014). doi: [10.1038/nano.2013.253](https://doi.org/10.1038/nano.2013.253); pmid: [24292513](https://pubmed.ncbi.nlm.nih.gov/24292513/)
- J. A. Liddle, Y. Cui, P. Alivisatos, Lithographically directed self-assembly of nanostructures. *J. Vac. Sci. Technol. B* **22**, 3409–3414 (2004). doi: [10.1116/1.1821572](https://doi.org/10.1116/1.1821572)
- S. O. Kim *et al.*, Epitaxial self-assembly of block copolymers on lithographically defined nanopatterned substrates. *Nature* **424**, 411–414 (2003). doi: [10.1038/nature01775](https://doi.org/10.1038/nature01775); pmid: [12879065](https://pubmed.ncbi.nlm.nih.gov/12879065/)
- R. A. Vega, D. Maspocho, K. Salaita, C. A. Mirkin, Nanoarrays of single virus particles. *Angew. Chem. Int. Ed.* **44**, 6013–6015 (2005). doi: [10.1002/anie.200501978](https://doi.org/10.1002/anie.200501978); pmid: [16114076](https://pubmed.ncbi.nlm.nih.gov/16114076/)
- P. Morales *et al.*, Suspending DNA origami between four gold nanodots. *Small* **12**, 169–173 (2016). doi: [10.1002/smll.201501782](https://doi.org/10.1002/smll.201501782); pmid: [26573881](https://pubmed.ncbi.nlm.nih.gov/26573881/)
- R. J. Kershner *et al.*, Placement and orientation of individual DNA shapes on lithographically patterned surfaces. *Nat. Nanotechnol.* **4**, 557–561 (2009). doi: [10.1038/nnano.2009.220](https://doi.org/10.1038/nnano.2009.220); pmid: [19734926](https://pubmed.ncbi.nlm.nih.gov/19734926/)
- T. D. Yuzvinsky, A. M. Fennimore, A. Kis, A. Zettl, Controlled placement of highly aligned carbon nanotubes for the manufacture of arrays of nanoscale torsional actuators. *Nanotechnology* **17**, 434–438 (2006). doi: [10.1088/0957-4484/17/2/015](https://doi.org/10.1088/0957-4484/17/2/015)
- B. Ding *et al.*, Interconnecting gold islands with DNA origami nanotubes. *Nano Lett.* **10**, 5065–5069 (2010). doi: [10.1021/nl1033073](https://doi.org/10.1021/nl1033073); pmid: [21070012](https://pubmed.ncbi.nlm.nih.gov/21070012/)
- Y. Huang, X. Duan, Q. Wei, C. M. Lieber, Directed assembly of one-dimensional nanostructures into functional networks. *Science* **291**, 630–633 (2001). doi: [10.1126/science.291.5504.630](https://doi.org/10.1126/science.291.5504.630); pmid: [11158671](https://pubmed.ncbi.nlm.nih.gov/11158671/)
- Y. Zhang *et al.*, Electric-field-directed growth of aligned single-walled carbon nanotubes. *Appl. Phys. Lett.* **79**, 3155–3157 (2001). doi: [10.1063/1.1415412](https://doi.org/10.1063/1.1415412)
- M. Tanase *et al.*, Magnetic alignment of fluorescent nanowires. *Nano Lett.* **1**, 155–158 (2001). doi: [10.1021/nl005532s](https://doi.org/10.1021/nl005532s)
- A. Kuzlyk, B. Yurke, J. J. Toppari, V. Linko, P. Törmä, Dielectrophoretic trapping of DNA origami. *Small* **4**, 447–450 (2008). doi: [10.1002/smll.200701320](https://doi.org/10.1002/smll.200701320); pmid: [18350556](https://pubmed.ncbi.nlm.nih.gov/18350556/)
- B. K. P. Horn, Closed-form solution of absolute orientation using unit quaternions. *J. Opt. Soc. Am. A* **4**, 629–642 (1987). doi: [10.1364/JOSAA.4.000629](https://doi.org/10.1364/JOSAA.4.000629)
- A. Gopinath, P. W. K. Rothmund, Optimized assembly and covalent coupling of single-molecule DNA origami nanoarrays. *ACS Nano* **8**, 12030–12040 (2014). doi: [10.1021/nl506014s](https://doi.org/10.1021/nl506014s); pmid: [25412345](https://pubmed.ncbi.nlm.nih.gov/25412345/)
- A. Gopinath, E. Miyazono, A. Faraon, P. W. K. Rothmund, Engineering and mapping nanocavity emission via precision bonding of DNA origami. *Nature* **535**, 401–405 (2016). doi: [10.1038/nature18287](https://doi.org/10.1038/nature18287); pmid: [27398616](https://pubmed.ncbi.nlm.nih.gov/27398616/)
- See supplementary materials.
- H. Dietz, S. M. Douglas, W. M. Shih, Folding DNA into twisted and curved nanoscale shapes. *Science* **325**, 725–730 (2009). doi: [10.1126/science.1174251](https://doi.org/10.1126/science.1174251); pmid: [19661424](https://pubmed.ncbi.nlm.nih.gov/19661424/)
- A. N. Marchi, I. Saaem, B. N. Vogen, S. Brown, T. H. LaBean, Toward larger DNA origami. *Nano Lett.* **14**, 5740–5747 (2014). doi: [10.1021/nl502626s](https://doi.org/10.1021/nl502626s)
- X. Xiong, S.-H. Liang, K. F. Böhringer, in *2004 IEEE International Conference on Robotics and Automation, 2004. Proceedings. ICRA '04 (2004)*, vol. 2, pp. 1141–1148. doi: [10.1109/ROBOT.2004.1307978](https://doi.org/10.1109/ROBOT.2004.1307978)
- A. Gopinath, D. Kirkpatrick, P. Rothmund, C. Thachuk, in *Proceedings of the 28th Canadian Conference on Computational Geometry (2016)*, pp. 230–236.
- S.-H. Liang, X. Xiong, K. F. Böhringer, in *17th IEEE International Conference on Micro Electro Mechanical Systems (MEMS 2004) (2004)*, pp. 9–12. doi: [10.1109/MEMS.2004.1290509](https://doi.org/10.1109/MEMS.2004.1290509)
- H. P. Spielmann, D. E. Wemmer, J. P. Jacobsen, Solution structure of a DNA complex with the fluorescent bis-intercalator TOTO determined by NMR spectroscopy. *Biochemistry* **34**, 8542–8553 (1995). doi: [10.1021/bi00027a004](https://doi.org/10.1021/bi00027a004); pmid: [7612596](https://pubmed.ncbi.nlm.nih.gov/7612596/)
- J. M. Schins, A. Agronskaia, B. G. de Groot, J. Greve, Orientation of the chromophore dipoles in the TOTO-DNA system. *Cytometry* **37**, 230–237 (1999). doi: [10.1002/\(SICI\)1097-0320\(19991101\)37:3<230::AID-CYTO10>3.0.CO;2-#](https://doi.org/10.1002/(SICI)1097-0320(19991101)37:3<230::AID-CYTO10>3.0.CO;2-#)
- M. L. Bennis *et al.*, Single-molecule manipulation of double-stranded DNA using optical tweezers: Interaction studies of DNA with RecA and YOYO-1. *Cytometry* **36**, 200–208 (1999). doi: [10.1002/\(SICI\)1097-0320\(19990701\)36:3<200::AID-CYTO9>3.0.CO;2-T](https://doi.org/10.1002/(SICI)1097-0320(19990701)36:3<200::AID-CYTO9>3.0.CO;2-T); pmid: [10404969](https://pubmed.ncbi.nlm.nih.gov/10404969/)
- F. Persson, F. Westerlund, J. O. Tegenfeldt, A. Kristensen, Local conformation of confined DNA studied using emission polarization anisotropy. *Small* **5**, 190–193 (2009). doi: [10.1002/smll.200800423](https://doi.org/10.1002/smll.200800423); pmid: [19072931](https://pubmed.ncbi.nlm.nih.gov/19072931/)
- T. Ha, T. A. Laurence, D. S. Chelma, S. Weiss, Polarization spectroscopy of single fluorescent molecules. *J. Phys. Chem. B* **103**, 6839–6850 (1999). doi: [10.1021/p990948j](https://doi.org/10.1021/p990948j)
- B. Sick, B. Hecht, L. Novotny, Orientational imaging of single molecules by annular illumination. *Phys. Rev. Lett.* **85**, 4482–4485 (2000). doi: [10.1103/PhysRevLett.85.4482](https://doi.org/10.1103/PhysRevLett.85.4482); pmid: [11082576](https://pubmed.ncbi.nlm.nih.gov/11082576/)
- Note that the strength of the net dipole moment is not the same as the net dipole strength. Consider equal and opposite dipoles  $\mu_1 = -\mu_2$  intercalated  $180^\circ$  from each other around the helix. They cancel to yield zero net dipole moment but contribute equally to the net dipole strength, and hence to emission under E.
- A. S. Backer, M. Y. Lee, W. E. Moerner, Enhanced DNA imaging using super-resolution microscopy and simultaneous single-molecule orientation measurements. *Optica* **3**, 659–666 (2016). doi: [10.1364/OPTICA.3.000659](https://doi.org/10.1364/OPTICA.3.000659)
- C. A. Valades Cruz *et al.*, Quantitative nanoscale imaging of orientational order in biological filaments by polarized superresolution microscopy. *Proc. Natl. Acad. Sci. U.S.A.* **113**, E820–E828 (2016). doi: [10.1073/pnas.1516811113](https://doi.org/10.1073/pnas.1516811113); pmid: [26831082](https://pubmed.ncbi.nlm.nih.gov/26831082/)
- N. Milanovich, M. Suh, R. Jankowiak, G. J. Small, J. M. Hayes, Binding of TO-PRO-3 and TO10-3 to DNA: Fluorescence and hole-burning studies. *J. Phys. Chem.* **100**, 9181–9186 (1996). doi: [10.1021/jp960062s](https://doi.org/10.1021/jp960062s)
- S. Pal *et al.*, DNA directed self-assembly of anisotropic plasmonic nanostructures. *J. Am. Chem. Soc.* **133**, 17606–17609 (2011). doi: [10.1021/ja207898r](https://doi.org/10.1021/ja207898r); pmid: [21981707](https://pubmed.ncbi.nlm.nih.gov/21981707/)
- M. Vyborny, A. L. Nussbaumer, S. M. Langenegger, R. Häner, Assembling multiporphyrin stacks inside the DNA double helix. *Bioconjug. Chem.* **25**, 1785–1793 (2014). doi: [10.1021/bc500297e](https://doi.org/10.1021/bc500297e); pmid: [25186936](https://pubmed.ncbi.nlm.nih.gov/25186936/)
- F. Afshinmanesh, J. S. White, W. Cai, M. L. Brongersma, Measurement of the polarization state of light using an integrated plasmonic polarimeter. *Nanophotonics* **1**, 125–129 (2012). doi: [10.1515/nanoph-2012-0004](https://doi.org/10.1515/nanoph-2012-0004)
- J. P. Balthasar Mueller, K. Leosson, F. Capasso, Ultracompact metasurface in-line polarimeter. *Optica* **3**, 42–47 (2016). doi: [10.1364/OPTICA.3.000042](https://doi.org/10.1364/OPTICA.3.000042)
- S. B. Mehta *et al.*, Dissection of molecular assembly dynamics by tracking orientation and position of single molecules in live cells. *Proc. Natl. Acad. Sci. U.S.A.* **113**, E6352–E6361 (2016). doi: [10.1073/pnas.1607674113](https://doi.org/10.1073/pnas.1607674113); pmid: [27679846](https://pubmed.ncbi.nlm.nih.gov/27679846/)
- O. Benson, Assembly of hybrid photonic architectures from nanophotonic constituents. *Nature* **480**, 193–199 (2011). doi: [10.1038/nature10610](https://doi.org/10.1038/nature10610); pmid: [22158243](https://pubmed.ncbi.nlm.nih.gov/22158243/)
- A. M. Armani, R. P. Kulkarni, S. E. Fraser, R. C. Flagan, K. J. Vahala, Label-free, single-molecule detection with optical microcavities. *Science* **317**, 783–787 (2007). doi: [10.1126/science.1145002](https://doi.org/10.1126/science.1145002); pmid: [17615303](https://pubmed.ncbi.nlm.nih.gov/17615303/)
- K. Hennessy *et al.*, Quantum nature of a strongly coupled single quantum dot-cavity system. *Nature* **445**, 896–899 (2007). doi: [10.1038/nature05586](https://doi.org/10.1038/nature05586); pmid: [17259971](https://pubmed.ncbi.nlm.nih.gov/17259971/)
- J. Friedrich-Möller *et al.*, Deterministic coupling of a single silicon-vacancy color center to a photonic crystal cavity in diamond. *Nano Lett.* **14**, 5281–5287 (2014). doi: [10.1021/nl502327b](https://doi.org/10.1021/nl502327b); pmid: [25111134](https://pubmed.ncbi.nlm.nih.gov/25111134/)
- C. Lethiec *et al.*, Measurement of three-dimensional dipole orientation of a single fluorescent nanoemitter by emission polarization analysis. *Phys. Rev. X* **4**, 021037 (2014). doi: [10.1103/PhysRevX.4.021037](https://doi.org/10.1103/PhysRevX.4.021037)
- A. Lyasota *et al.*, Integration of multiple site-controlled pyramidal quantum dot systems with photonic-crystal membrane cavities. *J. Cryst. Growth* **414**, 192–195 (2015). doi: [10.1016/j.jcrysgro.2014.10.028](https://doi.org/10.1016/j.jcrysgro.2014.10.028)
- M. Barth *et al.*, Nanoassembled plasmonic-photonic hybrid cavity for tailored light-matter coupling. *Nano Lett.* **10**, 891–895 (2010). doi: [10.1021/nl903555u](https://doi.org/10.1021/nl903555u); pmid: [20141157](https://pubmed.ncbi.nlm.nih.gov/20141157/)
- D. Englund *et al.*, Deterministic coupling of a single nitrogen vacancy center to a photonic crystal cavity. *Nano Lett.* **10**, 3922–3926 (2010). doi: [10.1021/nl101662v](https://doi.org/10.1021/nl101662v); pmid: [20825160](https://pubmed.ncbi.nlm.nih.gov/20825160/)
- R. J. Pfab *et al.*, Aligned terrylene molecules in a spin-coated ultrathin crystalline film of p-terphenyl. *Chem. Phys. Lett.* **387**, 490–495 (2004). doi: [10.1016/j.cplett.2004.02.040](https://doi.org/10.1016/j.cplett.2004.02.040)
- M. Lesik *et al.*, Perfect preferential orientation of nitrogen-vacancy defects in a synthetic diamond sample. *Appl. Phys. Lett.* **104**, 113107 (2014). doi: [10.1063/1.4869103](https://doi.org/10.1063/1.4869103)
- J. Michl *et al.*, Perfect alignment and preferential orientation of nitrogen-vacancy centers during chemical vapor deposition diamond growth on (111) surfaces. *Appl. Phys. Lett.* **104**, 102407 (2014). doi: [10.1063/1.4868128](https://doi.org/10.1063/1.4868128)
- S.-H. Lim, T. G. Bjorklund, F. C. Spano, C. J. Bardeen, Exciton delocalization and superradiance in tetracene thin films and nanoaggregates. *Phys. Rev. Lett.* **92**, 107402 (2004). doi: [10.1103/PhysRevLett.92.107402](https://doi.org/10.1103/PhysRevLett.92.107402); pmid: [15089241](https://pubmed.ncbi.nlm.nih.gov/15089241/)
- C. Hettich *et al.*, Nanometer resolution and coherent optical dipole coupling of two individual molecules. *Science* **298**, 385–389 (2002). doi: [10.1126/science.1075606](https://doi.org/10.1126/science.1075606); pmid: [12215651](https://pubmed.ncbi.nlm.nih.gov/12215651/)
- L. Novotny, From near-field optics to optical antennas. *Phys. Today* **64**, 47–52 (2011). doi: [10.1063/PT.3.1167](https://doi.org/10.1063/PT.3.1167)
- A. Alù, N. Engheta, Tuning the scattering response of optical nanoantennas with nanocircuit loads. *Nat. Photonics* **2**, 307–310 (2008). doi: [10.1038/nphoton.2008.53](https://doi.org/10.1038/nphoton.2008.53)
- A system with multiple local maxima and a single global maximum could break rotational symmetry in the limit of slow annealing to zero temperature. We have yet to find a practical way to anneal DOP, but a combination of heat and monovalent cations has been used to mobilize and crystallize origami kinetically trapped on mica (56).
- S. Woo, P. W. K. Rothmund, Self-assembly of two-dimensional DNA origami lattices using cation-controlled surface diffusion. *Nat. Commun.* **5**, 4889 (2014). doi: [10.1038/ncomms5889](https://doi.org/10.1038/ncomms5889); pmid: [25205175](https://pubmed.ncbi.nlm.nih.gov/25205175/)
- M. Decker, M. W. Klein, M. Wegener, S. Linden, Circular dichroism of planar chiral magnetic metamaterials. *Opt. Lett.* **32**, 856–858 (2007). doi: [10.1364/OL.32.000856](https://doi.org/10.1364/OL.32.000856); pmid: [17339960](https://pubmed.ncbi.nlm.nih.gov/17339960/)
- W. Ye *et al.*, Spin and wavelength multiplexed nonlinear metasurface holography. *Nat. Commun.* **7**, 11930 (2016). doi: [10.1038/ncomms11930](https://doi.org/10.1038/ncomms11930); pmid: [27306147](https://pubmed.ncbi.nlm.nih.gov/27306147/)
- C. Van Dyck, M. A. Ratner, Molecular rectifiers: A new design based on asymmetric anchoring moieties. *Nano Lett.* **15**, 1577–1584 (2015). doi: [10.1021/nl504091v](https://doi.org/10.1021/nl504091v); pmid: [25706442](https://pubmed.ncbi.nlm.nih.gov/25706442/)
- M. M. Shulaker *et al.*, Carbon nanotube computer. *Nature* **501**, 526–530 (2013). doi: [10.1038/nature12502](https://doi.org/10.1038/nature12502); pmid: [24067711](https://pubmed.ncbi.nlm.nih.gov/24067711/)
- S. M. Douglas *et al.*, Rapid prototyping of 3D DNA-origami shapes with cadNano. *Nucleic Acids Res.* **37**, 5001–5006 (2009). doi: [10.1093/nar/gkp436](https://doi.org/10.1093/nar/gkp436); pmid: [19531737](https://pubmed.ncbi.nlm.nih.gov/19531737/)
- <https://doi.org/10.5281/zenodo.4317480>

## ACKNOWLEDGMENTS

Fabrication was done at Caltech's Kavli Nanoscience Institute. **Funding:** Supported by Office of Naval Research awards N00014-1-1-0702 and N00014-17-1-2610, NSF grants 1636364 and 1317694 (Expedition in Computing, Molecular Programming Project, <http://molecular-programming.org>), Air Force Office of Scientific Research grant FA9550-16-1-0019 (A.M.), the Natural Sciences and Engineering Research Council of Canada (D.K.), a Banting Fellowship (C.T.), the Orr Family Foundation, and the Abedin Institute. **Author contributions:** A.G. and A.M. performed all experiments; A.G. performed Lumerical simulations; A.G. and P.W.K.R. analyzed primary experimental data; C.T. wrote software for thermodynamic and kinetic modeling and simulation; C.T. and P.W.K.R. performed analysis and comparison of experimental data with thermodynamic and kinetic predictions; C.T. and D.K. derived the small moon shape; A.G. and P.W.K.R. wrote the manuscript; and all authors edited the manuscript. **Competing interests:** A.G., C.T., D.K., and P.W.K.R. have filed a patent application based on this work. A.G. and P.W.K.R. are co-founders of Palamedix. **Data and materials availability:** All data needed to evaluate the conclusions in the paper are present in the paper or the supplementary materials. Software for kinetic, thermodynamic, and EM simulations, right triangle orientation analysis, as well as e-beam and DNA origami design files are present in the supplementary materials and on Zenodo (62).

## SUPPLEMENTARY MATERIALS

[science.sciencemag.org/content/371/6531/eabd6179/suppl/DC1](https://science.sciencemag.org/content/371/6531/eabd6179/suppl/DC1)  
Materials and Methods  
Figs. S1 to S17  
References (63–80)

2 July 2020; accepted 14 December 2020  
[10.1126/science.abd6179](https://doi.org/10.1126/science.abd6179)

## Absolute and arbitrary orientation of single-molecule shapes

Ashwin Gopinath, Chris Thachuk, Anya Mitskovets, Harry A. Atwater, David Kirkpatrick and Paul W. K. Rothemund

*Science* **371** (6531), eabd6179.  
DOI: 10.1126/science.abd6179

### Orienting origami binding

Directing self-assembly for devices will require placing nanocomponents not only in the correct position on a surface but also in particular orientations. Gopinath *et al.* designed an asymmetric DNA origami, a "small moon" shape that binds to lithographically patterned sites on silica to within 3° of a target orientation angle. The authors were able to position and orient a molecular dipole within the resonant mode of an optical cavity. More than 3000 DNA origami were arranged in a single fabrication step in 12 different orientations to create a simple polarimeter.

*Science*, this issue p. eabd6179

#### ARTICLE TOOLS

<http://science.sciencemag.org/content/371/6531/eabd6179>

#### SUPPLEMENTARY MATERIALS

<http://science.sciencemag.org/content/suppl/2021/02/17/371.6531.eabd6179.DC1>

#### REFERENCES

This article cites 78 articles, 9 of which you can access for free  
<http://science.sciencemag.org/content/371/6531/eabd6179#BIBL>

#### PERMISSIONS

<http://www.sciencemag.org/help/reprints-and-permissions>

Use of this article is subject to the [Terms of Service](#)

---

*Science* (print ISSN 0036-8075; online ISSN 1095-9203) is published by the American Association for the Advancement of Science, 1200 New York Avenue NW, Washington, DC 20005. The title *Science* is a registered trademark of AAAS.

Copyright © 2020 The Authors, some rights reserved; exclusive licensee American Association for the Advancement of Science. No claim to original U.S. Government Works